WWW.IJRPR.COM

International Journal of Research Publication and Reviews

Journal homepage: www.ijrpr.com ISSN 2582-7421

Finite-Element and Grey–RSM Optimization of Cold Deep Drawing for a Stainless-Steel Component

Chandrakant Sahu, Yogesh Kumar Deshmukh

Bharti Vishwavidyalaya Durg

ABSTRACT :

This thesis presents a simulation-driven, multi-response optimization of cold deep drawing for a stainless-steel cap using a hybrid Grey–Response Surface Methodology (Grey–RSM) built on finite-element analysis in ANSYS Workbench. Four controllable factors with direct shop-floor relevance were studied in a 27-run, three-level design: friction (μ), punch nose radius (R), punch displacement rate (v) and radial clearance (c). All parts (punch, die, holder, blank) were modeled as solid bodies; the blank used Stainless Steel NL (elastic–plastic), tools used Structural Steel (rigid behavior). A uniform mesh and large-deflection contact were adopted; the die was fixed, blank-holder pressure held constant, and the punch prescribed to the target draw height in a verified quasi-static regime. For each run, end-of-stroke fields equivalent elastic strain, equivalent plastic strain, von Mises stress, and total deformation were post-processed into three compact, smaller-the-better indices: PSI, EEI and EPR as an elastic–plastic partition indicator. Grey normalization produced a single Grey grade per run; a quadratic RSM (uncoded variables) modeled this grade for continuous optimization and ANOVA-based diagnostics.

Keywords: Deep drawing; Grey Relational Analysis; Response Surface Methodology; FEA; Modeling; Multi-Objective Optimization

Introduction

Deep drawing transforms a flat circular blank into a seamless cup by pushing it through a die opening with a punch while a blank-holder restrains the flange. The operation unfolds in stages. At the outset the flange feeds toward the die and bends over the die radius; as the punch advances, the wall forms and is pulled in axial tension while the flange remains in radial tension and hoop compression. The material simultaneously bends and unbends across the die and punch radii, which concentrates strain and often governs where failure initiates. The force–stroke response typically rises to a peak as bending, friction, and wall formation demand energy, may decline as steady drawing is established, and can rise again near bottoming because of reverse bending or incidental ironing if the die–punch clearance is tight. Process success is the balance between restraining the flange sufficiently to suppress wrinkling and allowing enough feed to avoid tearing. The blank-holder force, friction at the die/holder and punch interfaces, die and punch corner radii, die–punch clearance, and the initial blank diameter jointly determine this balance. Too little restraint allows circumferential buckles to develop in the flange; too much starvation elevates tensile strain in the wall and precipitates rupture near the die entry or punch nose. Clearance close to the sheet thickness promotes a free draw; tighter gaps introduce ironing that stabilizes thickness at the cost of force and heat, whereas generous gaps reduce force but make wrinkling control more sensitive to the holder strategy. Material anisotropy appears as earing circumferential height lobes aligned with rolling directions affecting trim allowance and efficiency; springback after unloading alters radii and angles, especially in high-strength or high-modulus sheets.

Material and Methods

This section details the modeling setup, meshing strategy, boundary conditions, and result extraction used to evaluate cold deep drawing of a stainless-steel circular cap via a finite-element (FE) model. All controllable factors are expressed in normalized form to ensure portability across gauges: friction coefficient (μ), punch nose radius (R), punch displacement rate (v), and die–punch radial clearance (c). The measurable outputs used for analysis are von Mises stress, equivalent plastic strain, equivalent elastic strain, and total deformation.

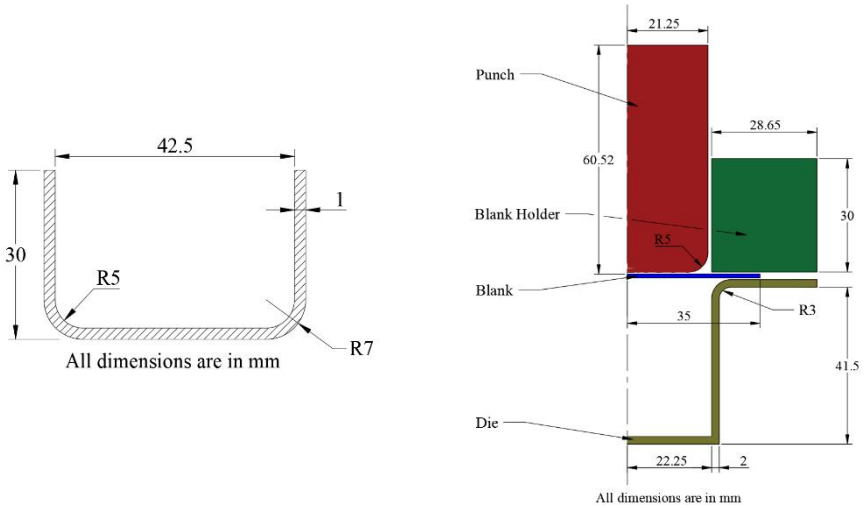

Figure 1. Detailed drawings of the finished part/component and deep drawing configuration

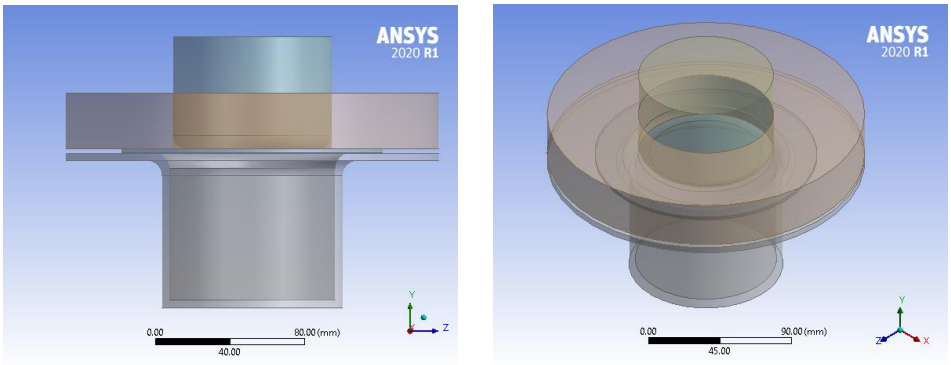

Figure 2. 3D Model of deep drawing configuration

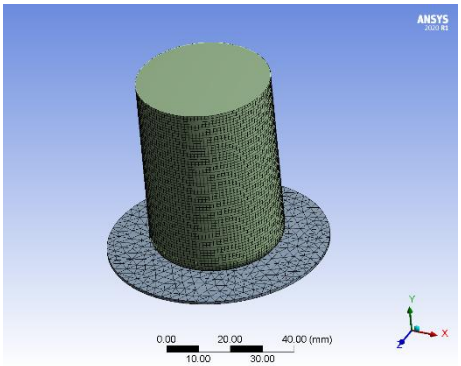

Figure 3. Meshed view of punch and blank component

All components the punch, die, blank-holder, and sheet blank were modeled as 3D solid bodies in ANSYS Workbench and discretized with a global element size of 1 mm. A high-order solid mesh was used (tetrahedral) so that curvature at the punch nose and die entry is accurately represented. On all contact faces, the surface node pitch was kept at 1 mm on both the tool and blank sides to stabilize contact tractions and avoid chattering during large deflection.

Table 1. Design factors and three-level settings for the deep-drawing DOE

Factor	Symbol	Levels		
		Level 1	Level 2	Level 3
Friction Coefficient, μ	$\boldsymbol{\mu}$	0.14	0.16	0.18
Punch Nose Radius, R_p	$\boldsymbol{R}$	5	7	9
Punch Displacement Rate, v	$\boldsymbol{v}$	3.5	5.5	7.5

Radial Clearance, c_r	***c***	0.2	0.3	0.4

Table 2. FE outputs and derived indices (PSI, EEI, EPR) for the 27-run deep-drawing DOE

Test Run	***μ***	***R***	***v***	***c***	**PSI**	**EER**	**EPR**
1	0.14	5	3.5	0.2	2000.3	0.749	0.000749
2	0.14	7	3.5	0.3	1394.5	0.369	0.000529
3	0.14	7	7.5	0.3	1742.8	0.728	0.000835
4	0.14	7	5.5	0.2	1525.4	0.490	0.000642
5	0.14	7	5.5	0.4	1609.2	0.601	0.000748
6	0.14	9	5.5	0.3	1469.0	0.393	0.000536
7	0.16	9	3.5	0.3	1516.6	0.428	0.000564
8	0.16	7	5.5	0.3	1798.5	0.775	0.000861
9	0.16	7	3.5	0.2	1570.9	0.524	0.000667
10	0.16	9	5.5	0.4	1738.4	0.667	0.000767
11	0.16	7	5.5	0.3	1799.3	0.775	0.000862
12	0.16	9	5.5	0.2	1652.0	0.552	0.000668
13	0.16	9	7.5	0.3	1881.3	0.802	0.000853
14	0.16	5	5.5	0.2	1857.1	0.886	0.000955
15	0.16	7	3.5	0.4	1658.1	0.640	0.000772
16	0.16	5	5.5	0.4	1949.9	1.014	0.001040
17	0.16	5	7.5	0.3	2101.9	1.168	0.001111
18	0.16	7	7.5	0.4	2039.3	1.046	0.001026
19	0.16	7	7.5	0.2	1943.3	0.915	0.000942
20	0.16	7	5.5	0.3	1795.7	0.771	0.000859
21	0.16	5	3.5	0.3	1713.5	0.745	0.000870
22	0.18	7	5.5	0.4	2096.0	1.096	0.001046
23	0.18	7	5.5	0.2	1997.9	0.962	0.000963
24	0.18	7	3.5	0.3	1850.3	0.818	0.000884
25	0.18	5	5.5	0.3	1937.0	0.848	0.000876
26	0.18	9	5.5	0.3	1939.0	0.850	0.000877
27	0.18	7	7.5	0.3	2250.0	1.250	0.001111

The Plastic Severity Index (PSI, MPa), Elastic Energy Index (EEI, MJ/m³), Elastic–Plastic Partition Ratio (EPR) can be calculated from below formula [23]:

$$PSI = \sigma \times e \quad \dots (1)$$

$$EEI = 0.5 \times \sigma \times \varepsilon \quad \dots (2)$$

$$EPR = \varepsilon \div e \quad \dots (3)$$

Result and Discussion

This chapter presents the results of a comprehensive study to optimize the cold deep drawing of a stainless-steel cap using a Grey–Response Surface Methodology (Grey–RSM) framework built on validated finite-element simulations in ANSYS Workbench. The objective is to identify process settings that minimize plastic-damage propensity and springback drivers while achieving the target draw without defects. To that end, the work systematically varies four practical factors—friction coefficient (μ), punch nose radius (R), punch displacement rate (v), and radial clearance (c) over three levels each in a 27-run design of experiments. The sheet blank is modeled as Stainless-Steel NL, the tools as Structural Steel, and the analysis extracts core field outputs (equivalent elastic strain, equivalent plastic strain, von Mises stress, total deformation) from which three compact, smaller-the-better indices are constructed: PSI (Plastic Severity Index), EEI (Elastic Energy Index), and EPR (Elastic–Plastic Partition Ratio). Grey analysis is applied to RSM-predicted responses to produce a single, auditable grade that ranks parameter combinations across competing criteria.

Table 3. ANOVA for GRG quadratic model

Source	DF	Adj SS	Adj MS	F-Value	P-Value
Model	14	0.739912	0.052851	21.09	0.000*
Linear	4	0.632244	0.158061	63.06	0.000*

μ	1	0.223495	0.223495	89.17	0.000*
R	1	0.144579	0.144579	57.68	0.000*
v	1	0.206995	0.206995	82.59	0.000*
c	1	0.013830	0.013830	5.52	0.037*
Square	4	0.012637	0.003159	1.26	0.338
μ*μ	1	0.006504	0.006504	2.60	0.133
R*R	1	0.000296	0.000296	0.12	0.737
v*v	1	0.001485	0.001485	0.59	0.456
c*c	1	0.002131	0.002131	0.85	0.375
2-Way Interaction	6	0.111029	0.018505	7.38	0.002*
μ*R	1	0.056917	0.056917	22.71	0.000*
μ*v	1	0.016816	0.016816	6.71	0.024*
μ*c	1	0.000023	0.000023	0.01	0.926
R*v	1	0.020247	0.020247	8.08	0.015*
R*c	1	0.004520	0.004520	1.80	0.204
v*c	1	0.000009	0.000009	0.00	0.954
Error	12	0.030077	0.002506		
Lack-of-Fit	10	0.030074	0.003007	1983.97	0.001*
Pure Error	2	0.000003	0.000002		
Total	26	0.769988			

*Significant

Figure 4. shows main-effects of each factor on GRG. The slope signs match the regression: GRG decreases with increasing μ and v, and increases with R and ccc within the tested range. The largest gradient is observed for μ and v, followed by R ; c exhibits a smaller but positive effect. This supports the process interpretation that reducing friction and softening punch curvature lower both plastic-damage and springback drivers. Figure 5.3 assesses residual normality for the GRG model. The points largely follow a straight line, indicating approximate normality of residuals. Minor tail departures are consistent with the significant lack-of-fit observed in ANOVA and suggest that additional curvature or design augmentation could further improve fit.

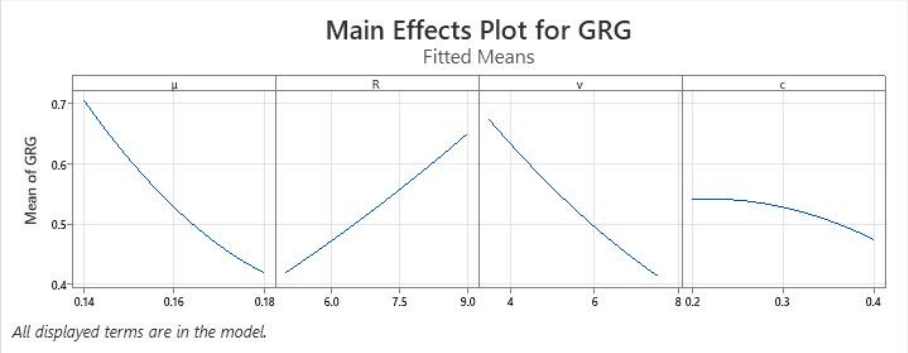

Figure 4. Main-effects on GRG

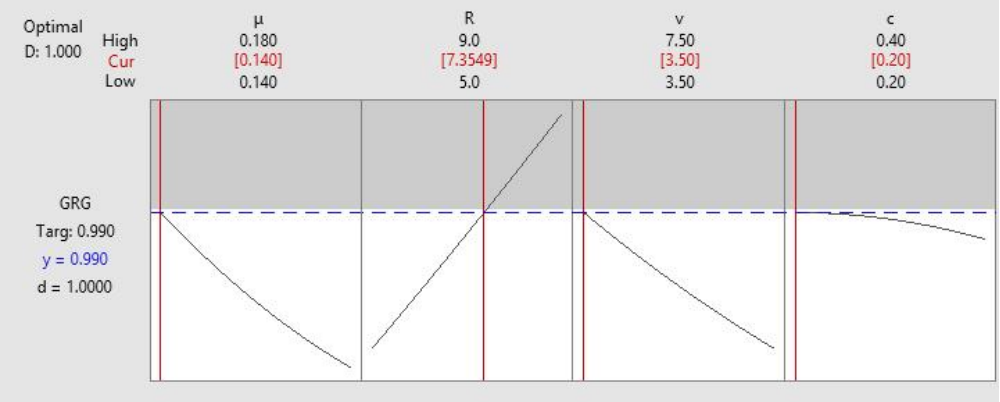

Figure 5. Optimization plot (desirability) continuous Grey–RSM optimum and predicted GRG with composite desirability

An optimization plot in Response Surface Methodology (RSM) is a graphical representation used to visualize the response surface and identify the optimal conditions that maximize or minimize the response variable of interest within the experimental design. After conducting the experiments and fitting a response surface model (often quadratic or higher-order models) to the data, the model equations are developed to represent the relationship between the factors and the response. The optimal combination results obtained from the GRG (Figure 5)

Conclusion

The results of the Grey–RSM optimization identify an optimum at approximately μ=0.14, R= 7.35 mm, v=3.5 mm/s and c=0.2 mm yielding a predicted Grey grade= 0.99. Relative to the baseline case, the confirmation simulation at this setting showed substantial reductions in the composite indices: PSI decreased by roughly one-third, EEI by about sixty percent, and EPR by around forty percent, all while achieving the target draw and maintaining stable contact and energy audits consistent with quasi-static assumptions. The agreement between predicted and observed Grey grades (within about 1%) validate both the metamodel and the optimization pathway. Collectively, these improvements indicate safer strain paths, reduced thinning/rupture risk, and lower springback propensity—precisely the qualities desired for robust production.

REFERENCES

1. Singh Sivam, S.P.S.; Rajendran, R.; Harshavardhana, N. (2024). An investigation of hybrid models FEA coupled with AHP-ELECTRE, RSM-GA, and ANN-GA into the process parameter optimization of high-quality deep-drawn cylindrical copper cups. Mechanics Based Design of Structures and Machines, 52(1), 498–522. https://doi.org/10.1080/15397734.2022.2120497
2. Cao, J.; Bambach, M.; Merklein, M.; Mozaffar, M.; Xue, T. (2024). Artificial intelligence in metal forming. CIRP Annals, 73(2), 561–587. https://doi.org/10.1016/j.cirp.2024.04.102
3. Lee, S.; Lim, Y.; Galdos, L.; Lee, T.; Quagliato, L. (2024). Gaussian process regression-driven deep drawing blank design method. International Journal of Mechanical Sciences, 265, 108898. https://doi.org/10.1016/j.ijmecsci.2023.108898
4. Han, S.; Kim, H. (2024). Artificial neural network-based sequential approximate optimization of metal sheet architecture and forming process. Journal of Computational Design and Engineering, 265–279. https://doi.org/10.1093/jcde/qwae049
5. Pegel, H.; Wycisk, D.; Sauer, D.U. (2023). Influence of cell dimensions and housing material on the energy density and fast-charging performance of tabless cylindrical lithium-ion cells. Energy Storage Materials, 60, 102796.
6. Moon, C.; Lian, J.; Lee, M. (2023). Identification of elastic and plastic properties of aluminum-polymer laminated pouch film for lithium-ion batteries: A hybrid experimental-numerical scheme. Journal of Energy Storage, 72, 108601.
7. Luyen, T.; Mac, T.; Banh, T.; Nguyen, D. (2023). Investigating the impact of yield criteria and process parameters on fracture height of cylindrical cups in the deep drawing process of SPCC sheet steel. International Journal of Advanced Manufacturing Technology, 128(5–6), 2059–2073.
8. Li, M.; Liu, X.; Kong, D.; Guo, Q.; Wang, Y.; Yao, J. (2023). Optimization of U-shaped flow channel by RBFNN and NSGA-II. International Journal of Mechanical Sciences, 243, 108012.
9. Géron, A. (2022). Hands-On Machine Learning with Scikit-Learn, Keras, and TensorFlow (3rd ed.). O'Reilly.
10. Li, K.; Wang, Y.; Chen, Z. (2022). A comparative study of battery state-of-health estimation based on empirical mode decomposition and neural network. Journal of Energy Storage, 54, 105333.
11. Tang, X.; Wang, Z.; Deng, L.; Wang, X.; Long, J.; Jiang, X.; Jin, J.; Xia, J. (2022). A review of the intelligent optimization and decision in plastic forming. Materials, 15(19), 7019. https://doi.org/10.3390/ma15197019
12. El Mrabti, I.; Touache, A.; El Hakimi, A.; Chamat, A. (2021). Springback optimization of deep drawing process based on FEM-ANN-PSO strategy. Structural and Multidisciplinary Optimization, 64(1), 321–333.
13. Xie, Y.; Du, L.; Zhao, J.; Liu, C.; Li, W. (2021). Multi-objective optimization of process parameters in stamping based on an improved RBM–BPNN network and MOPSO algorithm. Structural and Multidisciplinary Optimization, 64(6), 4209–4235.
14. Spathopoulos, S.C.; Stavroulakis, G.E. (2020). Springback prediction in sheet metal forming, based on finite element analysis and artificial neural network approach. Applied Mechanics, 1(2), 97–110.
15. Younas, N.; Chalal, H.; Abed-Meraim, F. (2020). Finite element simulation of sheet metal forming processes using non-quadratic anisotropic plasticity models and solid-shell finite elements. Procedia Manufacturing, 47, 1416–1423.
16. Montgomery, D.C. (2020). Design and Analysis of Experiments (10th ed.). Wiley.
17. Blank, J.; Deb, K. (2020). pymoo: Multi-Objective Optimization in Python. IEEE Access, 8, 89497–89509.
18. Barrett, T.J.; Knezevic, M. (2019). Deep drawing simulations using the finite element method embedding a multi-level crystal plasticity constitutive law: Experimental verification and sensitivity analysis. Computer Methods in Applied Mechanics and Engineering, 354, 245–270. https://doi.org/10.1016/j.cma.2019.05.035
19. Deng, J.; Sun, J.; Peng, W.; Hu, Y.; Zhang, D. (2019). Application of neural networks for predicting hot-rolled strip crown. Applied Soft Computing, 78, 119–131.
20. Li, L.; Jamieson, K.; DeSalvo, G.; Rostamizadeh, A.; Talwalkar, A. (2018). Hyperband: A novel bandit-based approach to hyperparameter optimization. arXiv preprint arXiv:1603.06560.
21. Amree, C.; Chaijit, S. (2018). Strain hardening analysis of SUS304 stainless steel cup for multi-stage deep drawing using finite element simulation—comparison with experiment result. 2nd International Conference on Engineering Innovation (ICEI 2018), 35–41. https://doi.org/10.1109/ICEI18.2018.8448624

22. Coër, J.; Laurent, H.; Oliveira, M.C.; Manach, P.; Menezes, L.F. (2018). Detailed experimental and numerical analysis of a cylindrical cup deep drawing: Pros and cons of using solid-shell elements. International Journal of Material Forming, 11(3), 357–373.

23. Hibbeler, R.C. (2017). Mechanics of Materials (10th ed.). Pearson.

24. Irthiea, I.K.; Green, G. (2017). Evaluation of micro deep drawing technique using soft die—simulation and experiments. International Journal of Advanced Manufacturing Technology, 89(5–8), 2363–2374.

25. Torabi, S.H.R.; Alibabaei, S.; Bonab, B.B.; Sadeghi, M.H.; Faraji, G. (2017). Design and optimization of turbine blade preform forging using RSM and NSGA-II. Journal of Intelligent Manufacturing, 28(6), 1409–1419.

26. Abadi, M.; Agarwal, A.; Barham, P.; Brevdo, E.; Chen, Z.; Citro, C.; Corrado, G.S.; Davis, A.; Dean, J.; Devin, M.; … Zheng, X. (2016). TensorFlow: Large-scale machine learning on heterogeneous distributed systems. arXiv preprint arXiv:1603.04467.

27. Reddy, A.C. (2015). Parametric significance of warm drawing process for 2024-T4 aluminum alloy through FEA. International Journal of Science and Research, 4(4), 2345–2351.

28. Xothapalli, C.; Reddy, A.C. (2015). Parametric importance of warm deep drawing process for 1070 aluminum alloy: Validation through FEA. International Journal of Scientific & Engineering Research, 6(4).

29. Thirunagari, S.; Reddy, A.C. (2015). Parametric optimization of warm deep drawing process of 1100 aluminum alloy: Validation through FEA. International Journal of Scientific & Engineering Research, 6(4), 425–435.

30. Reddy, A.C. (2015). Formability of superplastic deep drawing process with moving blank holder for AA1050-H18 conical cups. International Journal of Research in Engineering and Technology, 4(8), 124–132.

31. Reddy, A.C. (2015). Homogenization and parametric consequence of warm deep drawing process for 1050A aluminum alloy: Validation through FEA. International Journal of Science and Research, 4(4), 2034–2042.

32. Balla, Y.; Reddy, A.C. (2015). Parametric merit of warm deep drawing process for 1080A aluminium alloy: Validation through FEA. International Journal of Scientific & Engineering Research, 6(4).

33. Ciancio, C.; Citrea, T.; Ambrogio, G.; Filice, L.; Musmanno, R. (2015). Design of a high performance predictive tool for forging. Procedia CIRP, 33, 173–178.

34. Irthiea, I.K. (2014). Process analysis and design in micro deep drawing utilizing a flexible die. PhD thesis, University of Glasgow.

35. Brabie, G.; Costache, E.M.; Nanu, N.; Chirița, V. (2013). Prediction and minimisation of sheet thickness variation during deep drawing of micro/milli parts. International Journal of Mechanical Sciences, 68, 277–290.